Nuclear Instruments and Methods in Physics Research A 1075 (2025) 170394

Contents lists available at ScienceDirect

Nuclear Inst. and Methods in Physics Research, A

journal homepage: www.elsevier.com/locate/nima

Optimization and testing of microfocus pulsed X-ray source

Jiaxin Bai [a], Yunpeng Liu [a,b,*], Junxu Mu [a], Sheng Lai [a], Hao Yu [a], Ao Xia [a], Kang Wang [a], Xiaobin Tang [a,b,**]

[a] Department of Nuclear Science and Technology, Nanjing University of Aeronautics and Astronautics, Nanjing, 210016, China
[b] Key Laboratory of Advanced Nuclear Technology and Radiation Protection, Ministry of Industry and Information Technology, Nanjing, 210016, China

ARTICLE INFO

Keywords:
Pulsed X-ray
Microfocus
NSGA-II
Grid control
Open X-ray source

ABSTRACT

Pulsed X-ray sources have applications in laser additive manufacturing monitoring, high-speed X-ray imaging, distributed pulsed X-ray systems, X-ray elastic imaging, and X-ray communication. In this paper, we propose a hot-cathode pulsed micro-focus X-ray source (PMFX) with multiple focusing electrodes. The source has been optimized using the CST-MATLAB joint simulation method, with the objective of achieving small focal spot, high tube current, low cut-off voltage, and excellent modulation performance. Simulation results show that the focal spot of the PMFX can be reduced to 45 μm × 25 μm and 6 μm × 20 μm at cut-off voltages of −11 V and −23 V, respectively, with corresponding relative tube currents of 35% and 48%. The current, pulse performance, and focal spot size of the structure with two focusing electrodes were tested in a dynamic vacuum system. The minimum effective focal spot was measured to be 285 μm × 53 μm at 25 kV, with an anode current of 98 μA, consistent with the trend observed in the simulation results. Additionally, an X-ray pulse frequency of 840 kHz was achieved.

1. Introduction

Pulsed X-ray sources generate X-rays in the form of short pulses, and the pulse frequency can exceed 100 kHz. By adjusting the parameters of the X-ray source, the energy and frequency of the pulsed X-rays can be tailored to meet various experimental needs and applications. These sources are used for laser additive manufacturing monitoring [1], high-speed X-ray imaging, distributed pulsed X-ray systems [2], X-ray elastic imaging [3], and X-ray communication.

Currently, the main types of modulated X-ray sources are light-controlled modulated X-ray tubes (LMXTs) [4,5] and grid-controlled modulated X-ray tubes (GMXTs) [6–8]. These sources control the intensity of X-rays by adjusting the light source or the grid voltage, thereby achieving the emission of high-frequency pulses. Notably, the effective focal spot size of the X-ray source directly affects the spatial resolution of X-ray imaging. A smaller focal spot reduces imaging artifacts [9] and produces clearer images. For high temporal and spatial resolution X-ray imaging, the X-ray source should exhibit both a high-speed pulse emission repetition frequency and a focal spot size on the order of microns. However, previous studies on modulated X-ray sources have not emphasized the need for smaller focal spot size [10–14].

This study presents the design of a hot-cathode pulsed micro-focus X-ray source (PMFX) with multi-stage focusing. To meet the dual requirements of temporal and spatial resolution in high-speed X-ray imaging, the design optimized the structure of the X-ray source to achieve an ideal balance between high pulse emission repetition frequency and micrometer-scale focal spot. The X-ray source was modeled using the electromagnetic simulation program CST Particle Studio, and the structure design was optimized using the NSGA-II algorithm. In addition, a test platform for the X-ray source was constructed in a dynamic vacuum system to comprehensively evaluate the performance of the PMFX.

2. Simulation and optimization

2.1. Structure of PMFX

The X-ray source used in our laboratory is a grid-controlled modulated X-ray tube (GMXT) with a three-electrode structure, comprising a cathode, grid, and anode [14]. In this paper, focusing electrodes are introduced between the grid and the anode to decrease the focal spot size. The structure of the PMFX consists mainly of a reflective anode

* Corresponding author. Department of Nuclear Science and Technology, Nanjing University of Aeronautics and Astronautics, Nanjing, 210016, China.
** Corresponding author. Department of Nuclear Science and Technology, Nanjing University of Aeronautics and Astronautics, Nanjing, 210016, China.
E-mail addresses: liuyp@nuaa.edu.cn (Y. Liu), tangxiaobin@nuaa.edu.cn (X. Tang).

https://doi.org/10.1016/j.nima.2025.170394
Received 24 August 2024; Received in revised form 28 February 2025; Accepted 28 February 2025
Available online 28 February 2025

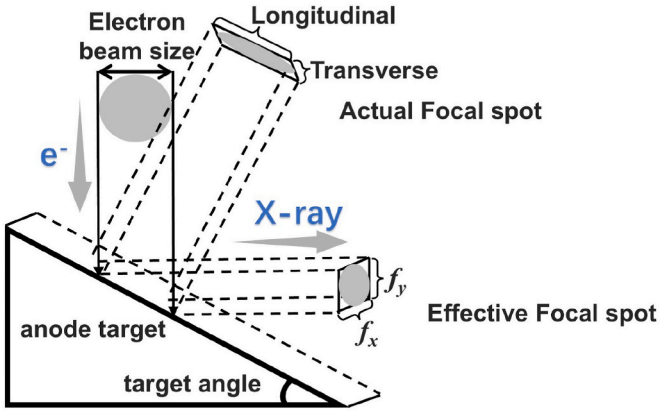

Fig. 1. Electron beam bombards anode target to produce X-rays, and actual and effective focal spots are obtained.

target, two focusing electrodes, a grid, a cathode shield, and a thermal cathode filament. The focusing electrodes have a circular aperture, and their loading voltages are adjusted to regulate the shape of the electron beam and the focal spot size. Two or three focusing electrodes are arranged to a multi-stage design of PMFX. We chose multi-stage focusing because it is more convenient to control the current and focusing point separately. Meanwhile, too many focusing electrodes would increase the cost and difficulty of control. Considering the practicality of the X-ray tube, we chose two or three focusing electrodes. The grid is designed with a groove shape. By adjusting the grid voltage, the electron beam can be controlled, thereby enabling the X-rays to be turned on and off as required.

2.2. Simulation method and key parameters selection

In this study, the three-dimensional electromagnetic analysis software CST was used to simulate the geometrical-optical characteristics of a PMFX. In this paper, the simulation module used is CST particle studio. The basic simulation process is as follows: draw structural model, set the structural material, set the boundary conditions, mesh, select the particle tracking solver, and start the calculation. After the completion of the solver, the results are obtained, including the number of particles, particle tracking, electric field distribution, and other results. The simulation results focused on four key indices: tube current (I), actual anode focal spot (as shown in Fig. 1), grid cut-off voltage (U_{cut}), and pulse response time (T). The number of anode electrons (N_e), is proportional to the tube current; therefore, the relative anode current is represented as the percentage of anode electrons relative to the total electrons emitted by the cathode. U_{cut} is defined as the grid voltage when the tube current is zero and plays a critical role in determining the complexity of the pulse control circuit. Due to the uneven initial distribution of electric fields and electrons, the dispersion time of cathode electrons to the anode, referred to as the pulse response time, affects the pulse frequency. This study is to design a pulsed microfocus X-ray source and to verify the feasibility of high-speed pulsed X-ray applied to X-ray imaging. For PMFX, the anode voltage was set to 25 kV.

Key parameters need to be screened before optimization. As shown in Fig. 2, the anode focal spot size varies with changes in the inner diameter of the focusing electrode (d_{focus}). Initially, the focal spot decreases as d_{focus} is adjusted, but it subsequently increases. By optimizing the structure parameters, the smallest possible focal spot for the given structure can be determined.

Since the U_{cut} calculated from the simulation of the PMFX is consistently within −60 V, the grid voltage is not taken as an optimization objective. However, the optimization process will prioritize selecting the lowest U_{cut}. Parameter sweeping was performed for each structure parameter using CST. We performed parameter sweeping by calculating the trend of the focal spot and U_{cut} when a parameter is varied linearly over a certain range. When the width of the grid opening (w_{grid}) and the depth of the grid opening (d_{grid}) are varied, the variations of N_e, T and focal spot size are shown in Fig. 3. The corresponding

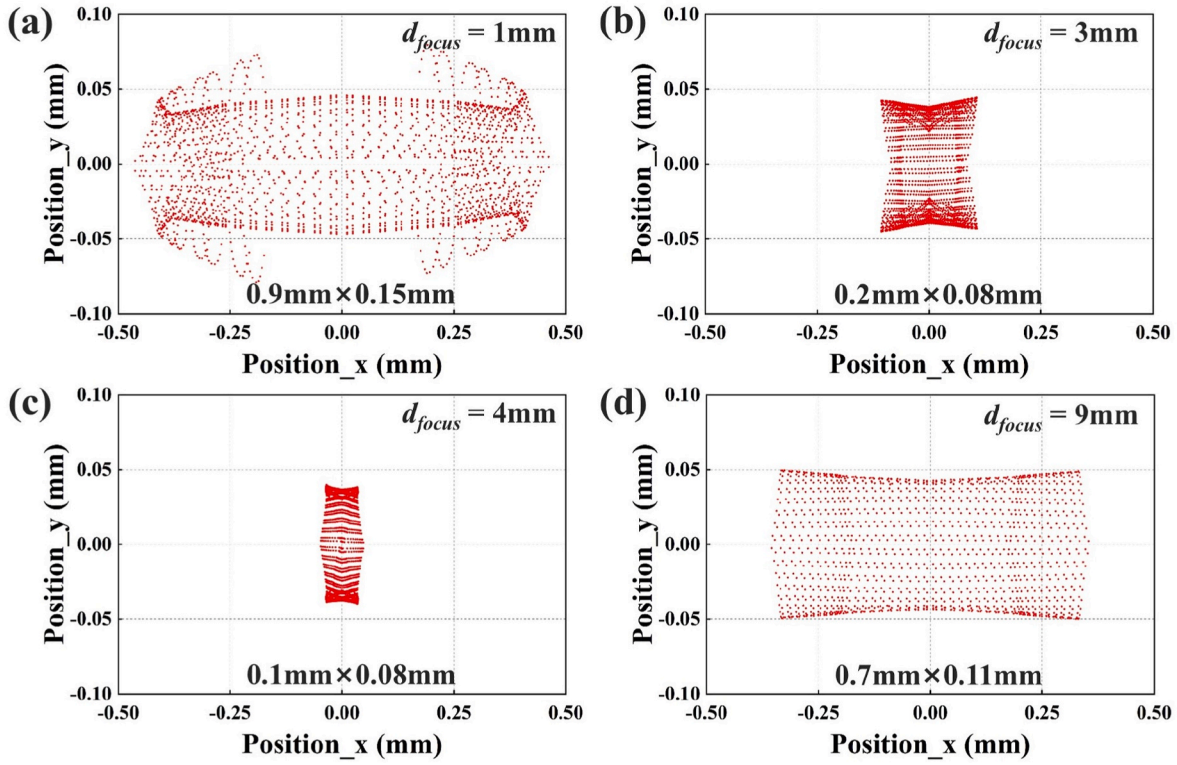

Fig. 2. Focal spot (a–d) as the inner diameter of the focusing electrode is varied.

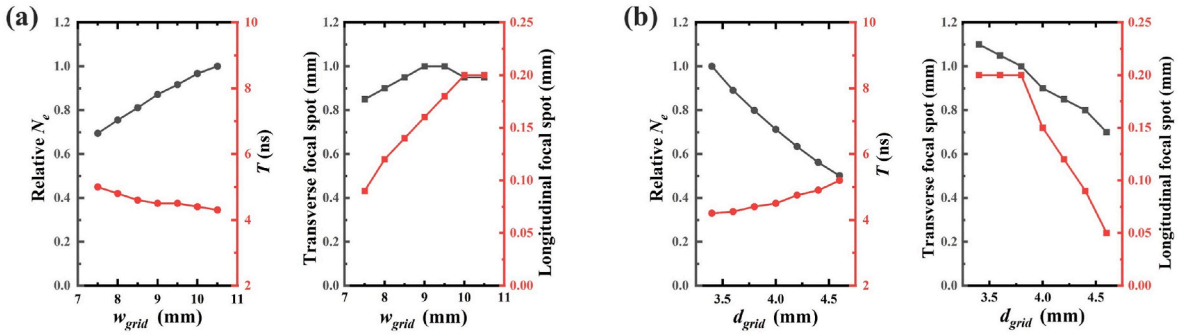

Fig. 3. Influence of (a) w_{grid} and (b) d_{grid} on normalized number of anode electrons N_e and pulse response time T (left) and transverse and longitudinal size of focal spot (right).

Table 1
Variation range of simulation results caused by change of structure parameters.

variation range	Parameter (mm)	Relative N_e	T (ns)	Transverse focal spot (mm)	Longitudinal focal spot (mm)
$h_{cathode}$	0.76–0.88	0.64–1	4.5–4.1	0.90–1.00	0.12–0.23
w_{grid}	7.5–10.5	0.69–1	5.0–4.3	0.85–0.95	0.09–0.20
d_{grid}	3.4–4.6	1~0.51	4.2–5.2	1.10–0.70	0.20–0.05
x_{focus}	1~7	1~0.53	4.2–5.6	1.10–0.50	0.20–0.04
d_{focus}	2~8	1~0.66	4.3–4.8	0.60–0.10	0.08–0.08

changes in these parameters for previous structure configurations are listed in Table 1. The pulse response time T varies on the order of nanoseconds and has minimal effect on the PMFX. Therefore, T is also not considered as an optimization objective. Instead, structure parameters that cause significant changes in N_e and the focal spot size were selected as key parameters. The final optimized key parameters are shown in Fig. 4, with a secondary focusing electrode structure used as an example.

2.3. Combined optimization with NSGA-II and CST

The NSGA-II is a multi-objective genetic algorithm based on non-dominated sorting [14–16]. NSGA-II generates random parameters

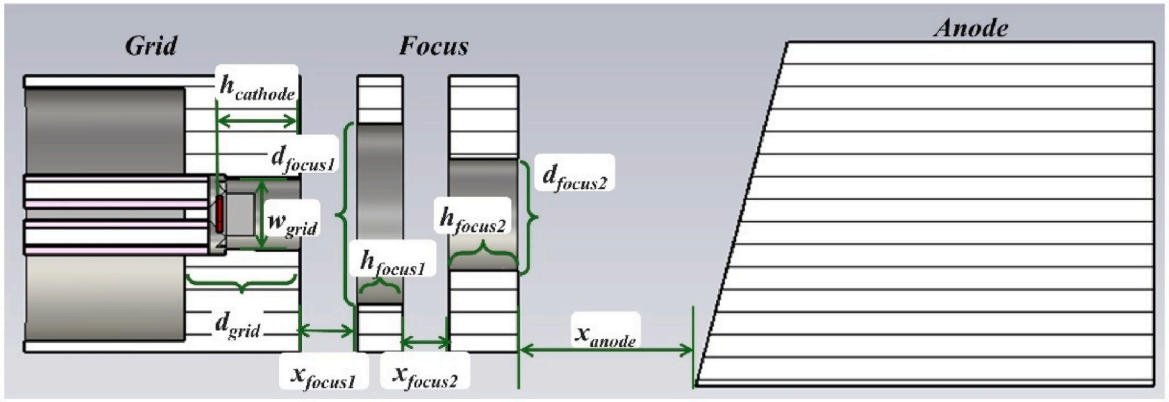

Fig. 4. Axial cross-section of structure of pulsed microfocus X-ray source with two focusing electrodes.

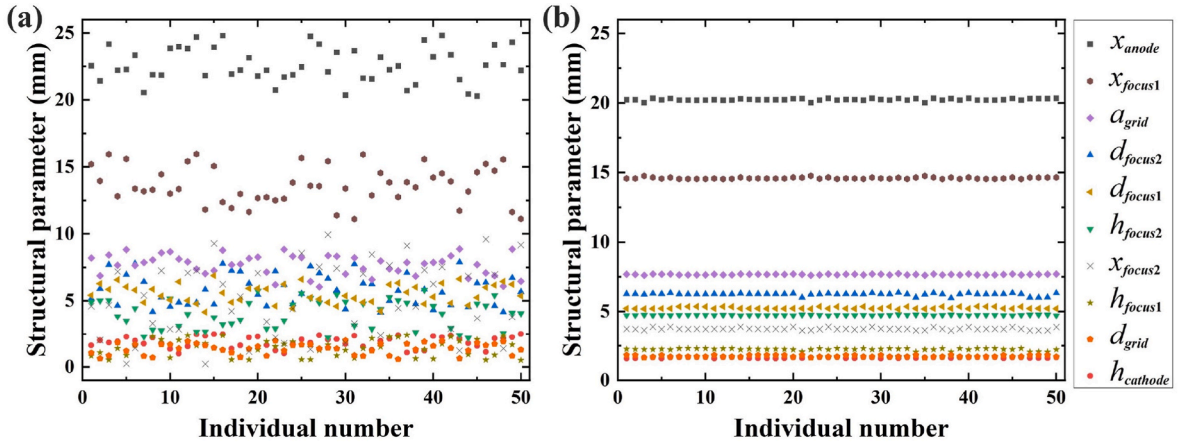

Fig. 5. Distribution of structure parameters of (a) initial and (b) final population. There are 50 samples in this population.

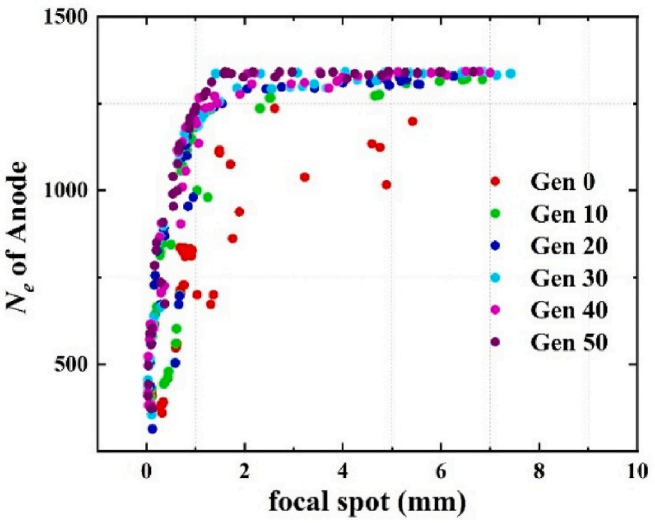

Fig. 6. Objective function front (N_e × focal spot) for sample size of 50.

Table 2
SP of solution.

Gen	0	10	20	30	40	50
SP	0.05638	0.02263	0.01828	0.01531	0.01513	0.01395

within a certain range. CST is invoked by MATLAB and then uses these parameters to simulate. The simulation results are returned and iterated for optimization.

The parameters of this model are optimized by using MATLAB-CST software co-simulation and NSGA-II multi-objective optimization algorithm, the decision variables and optimization objectives need to be determined. The decision variables are the key parameters calculated in Section 2.2, while the optimization objectives are the key indices of the simulation results. For the PMFX, the optimization objectives are focal spot size and N_e, limiting U_{cut} greater than −60 V. The optimization process was conducted for structures with both two and three focusing electrodes, with the two-electrode structure used as an example in the following optimization process.

2.4. Optimization results and discussion

When key structure parameters are used as optimizable variables, the range of values for each key parameter is determined based on the feasibility of the structure design. As shown in Fig. 5(a), the initial population distribution of each structure parameter was generated using NSGA-II. The structure parameters are randomly generated and uniformly sampled within the defined range of limit values. After 50 generations of optimization, as depicted in Fig. 5(b), all the structure parameters converged to fixed values. The objective functions formed a smooth Pareto front, as depicted in Fig. 6. The calculation results on the Pareto front are closest to the optimization objective. Selecting an appropriate solution from the optimal solution set is necessary based on actual requirements. The SP value [17] is used to measure the standard deviation of the minimum distance from each solution to the other solutions, reflecting the uniformity of the distribution of the solutions. A low SP value means that the solution is evenly distributed. We calculated the SP values for the results from generation 0 to 50 shown in Table 2. The number of iterations increases, the Spacing decreases and the solutions are more evenly distributed.

In this study, the final structure parameters were determined based on the Pareto front obtained from the optimization, ensuring that the optimization objectives were met. Fig. 7 shows the minimum focal spot obtained by optimizing the structure with two or three focusing electrodes. For the structure with two focusing electrodes, the minimum focal spot is 45 × 25 μm at 25 kV anode voltage, with U_{cut} at −11 V and N_e at 35% of the maximum. For the structure with three focusing electrodes, the minimum focal spot is 6 × 20 μm at 25 kV anode voltage, with U_{cut} at −23 V and N_e at 48% of the maximum. The corresponding structure parameters for these two configurations are shown in Table 3. Due to the limitation of the electrode columns number and chamber depth of the dynamic vacuum system, a PMFX structure with three focusing electrodes could not be accommodated, only the structure with two focusing electrodes was selected for testing to evaluate the DC

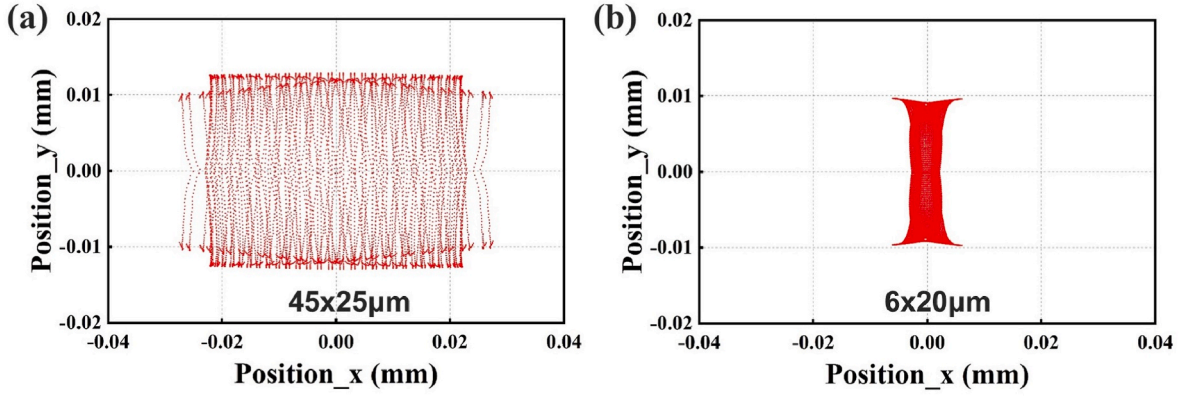

Fig. 7. Minimum anode focal spot size obtained by optimization (a) structure of two focusing electrodes (b) structure of three focusing electrodes.

Table 3
Two groups of optimized parameters.

Structure\Dimension (mm)		$h_{cathode}$	w_{grid}	d_{grid}	$x_{focus\ 1/2/3}$	$d_{focus\ 1/2/3}$	$h_{focus\ 1/2/3}$	$U_{focus1/2/3}(V)$
2 focusing electrodes	First	1.00	5.03	6.88	5.40	15.70	5.60	1050
	Second				13.96	9.70	14.70	680
3 focusing electrodes	First	1.68	5.36	6.65	11.10	4.90	9.78	3000
	Second				14.94	5.01	10.57	1820
	Third				3.12	2.04	4.98	1150

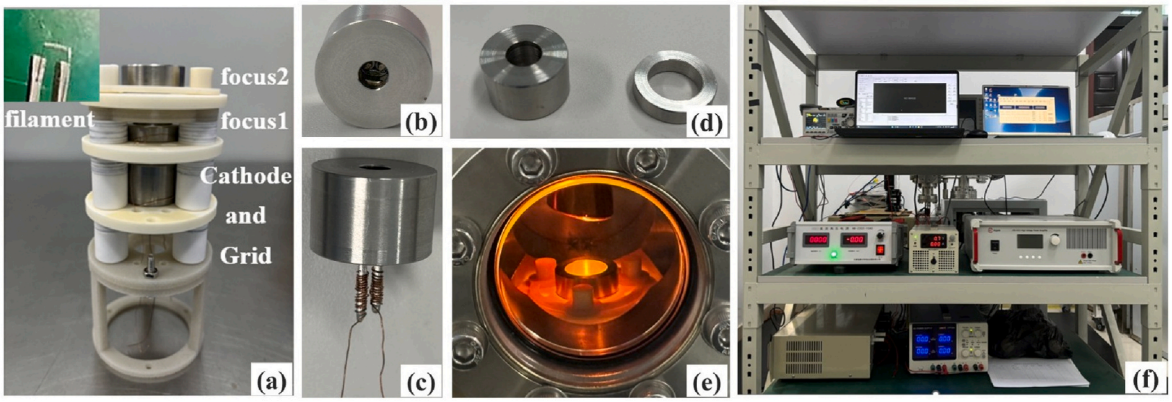

Fig. 8. X-ray source assembly. (a) Test structure components. (b) and (c) Cathode and grid module. (d) Focusing electrodes. (e) Observation window during filament operation. (f) Dynamic vacuum system test platform.

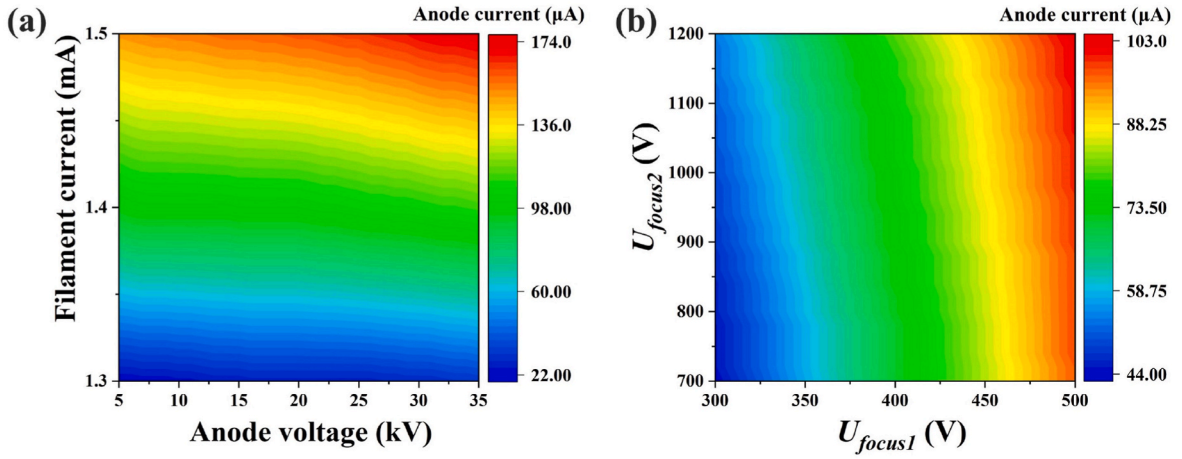

Fig. 9. Anode current variation (a) at different filament current and anode voltage, (b) at different U_{focus1} and different U_{focus2}.

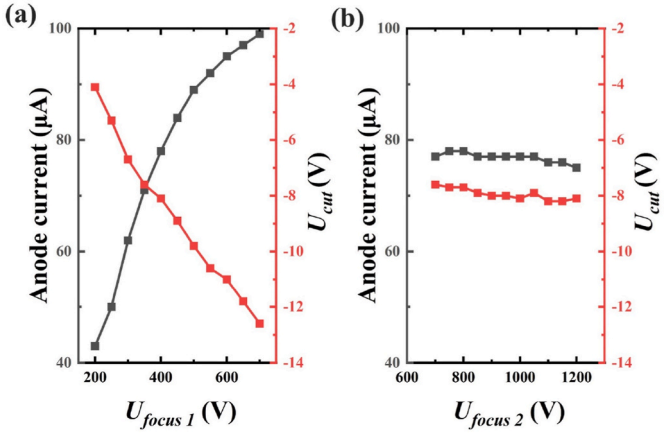

Fig. 10. Anode current and cut-off voltage at different U_{focus1} and U_{focus2}.

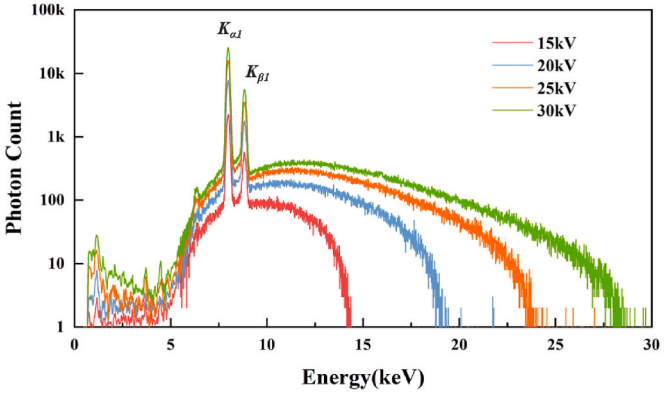

Fig. 11. X-ray source spectrum.

emission characteristics, pulsed emission characteristics, and focal spot size of the X-ray source.

3. Experiments

3.1. Experimental methodology

An experiment with a PMFX was carried out in a dynamic vacuum system [18]. As shown in Fig. 8, a spiral tungsten filament was used as the cathode, while the grid and focusing electrodes were made of stainless steel. The tungsten filament was attached to one end of a nickel rod plane via resistance welding, with the nickel rod isolated from the grid by a ceramic ring. All electrodes of the X-ray source, along with the flange electrode columns, were interconnected by pure copper wires. The anode target material was pure copper, and all other support materials were ceramic. To adjust the distance between the electrodes, customized ceramic spacers of varying thicknesses were used. Due to

Fig. 12. Focal spot measurement device (a) Imaging arrangement (b) Physical Tungsten sphere.

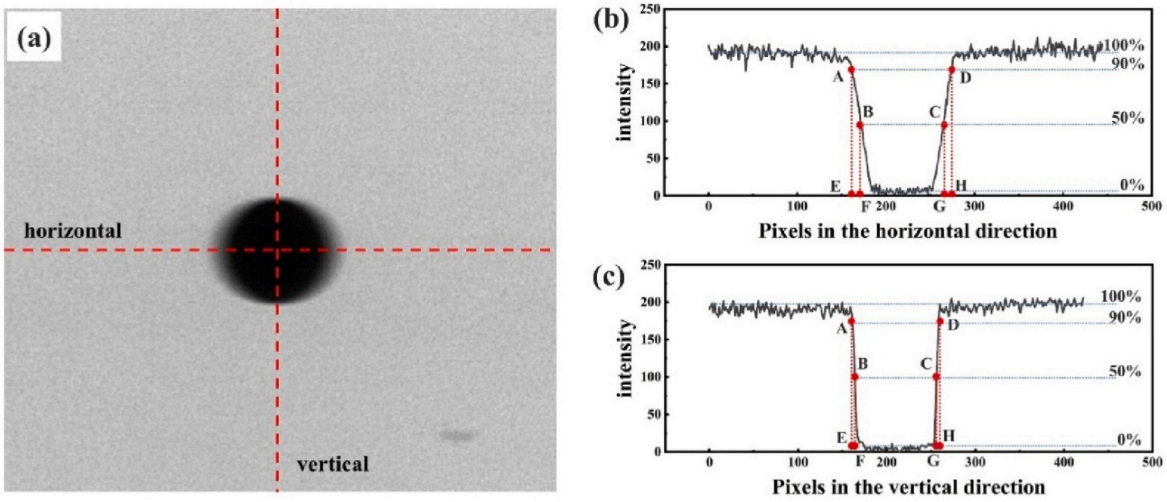

Fig. 13. (a) X-ray imaging of a tungsten sphere (b) Intensity distribution along the transverse direction (c) Intensity distribution along the longitudinal direction.

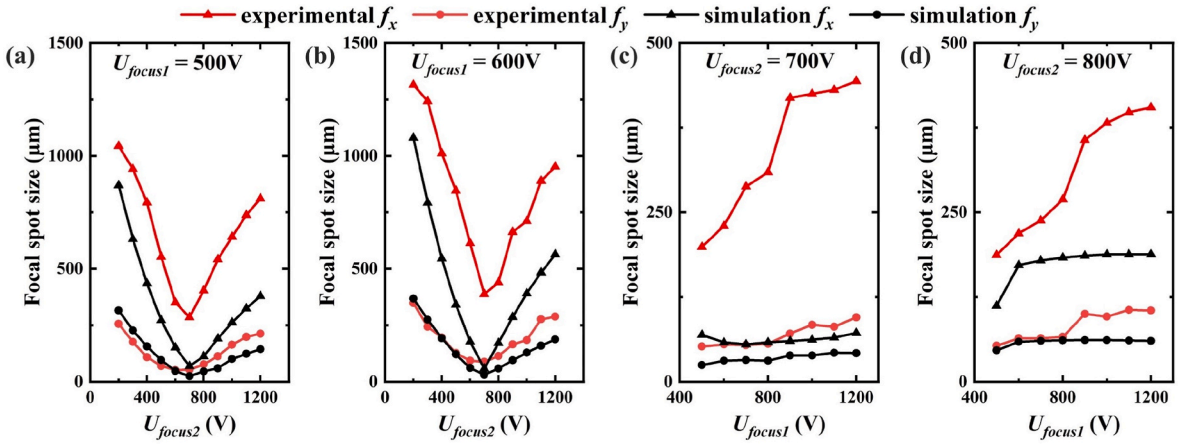

Fig. 14. Transverse and longitudinal focal spot size.

potential errors in distance control, the electrodes spacings were measured and recorded after assembly.

3.2. Experimental results and discussion

3.2.1. DC emission characteristics test

The anode current was tested under different conditions of filament current ($I_{cathode}$), anode voltage, focusing electrode 1 voltage (U_{focus1}) and focusing electrode 2 voltage (U_{focus2}). As shown in Fig. 9(a), at the same anode voltage, the anode current doubled when the filament current increased from 1.3 A to 1.4 A. Additionally, at a constant filament current, increasing the anode voltage from 5 kV to 35 kV resulted in a rise in anode current by 10–30 μA. Positive correlation is obvious. It means that the X-ray tube is operated in the non-saturation region. In Fig. 9(b), as U_{focus1} increased from 300 V to 500 V, the anode current also increased. When the U_{focus2} is increased from 700 V to 1200 V, the anode current increases slightly. This indicates that electrodes closer to the cathode have a greater influence on the anode current than those further

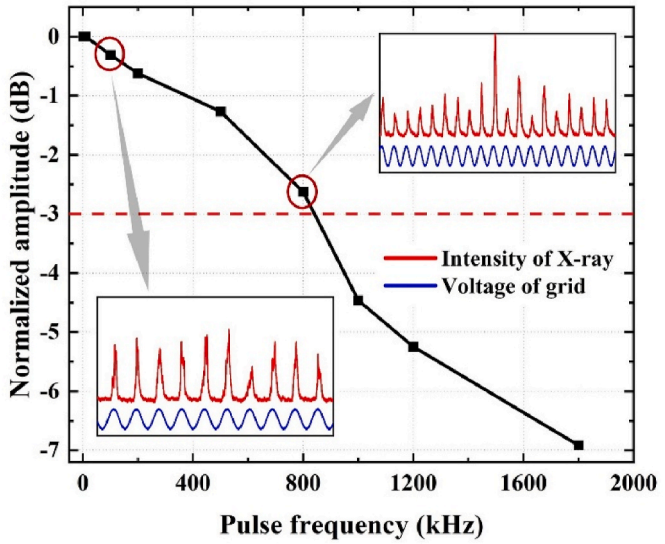

Fig. 15. X-ray frequency response curves, pulse waveforms at 100 kHz and 800 kHz, the blue line is the voltage waveform of the power amplifier input to the grid, and the red line is the X-ray waveform. (For interpretation of the references to colour in this figure legend, the reader is referred to the Web version of this article.)

away. This is due to the uneven distribution of the electric field inside the ray source, and the relatively high electric field intensity of the cathode attachment. When the electrode voltage near the cathode changes, it is easier to change the electric field distribution in the region, affecting the electron acceleration process, and thus easier to affect the anode current.

As shown in Fig. 10, the anode current and U_{cut} were recorded at different focusing electrode voltages. The measured U_{cut} values were all within the range of −20 to 0 V. In Fig. 10(a), the negative U_{cut} increases with the rise in U_{focus1}, while Fig. 10(b) shows U_{cut} is almost unaffected by U_{focus2}. Results indicate that, when U_{focus1} is increased, the anode current is increased. The increase in anode current essentially means that more electrons are accelerated towards the anode target. The rise in negative U_{cut} can increase the potential difference between the cathode and the grid, thereby cutting off the electrons completely.

3.2.2. X-ray spectrum test

We measured the X-ray source spectrum from 15 kV to 30 kV. To determine the spectra, we used a compact integrated spectrometer system (XR-100SDD), which consists of a silicon drift X-ray detector, a preamplifier, a digital pulse processor, and a multichannel analyzer. The obtained X-ray source spectrum is shown in Fig. 11, where K-series peaks of the Copper (Cu) material can be seen.

3.2.3. Focal spot test

The tungsten sphere was placed at the exit window of the X-ray source [19]. A flat-panel detector with 100 μm pixel was used to take the picture. The magnification M was controlled by adjusting the position of the flat-panel detector. In this experiment, M was about 10. X-ray image of the tungsten sphere was taken to obtain an image containing the X-ray intensity information as shown in Fig. 12. As shown in Fig. 13, the X-ray intensity distribution in the horizontal and vertical directions is obtained from the contrast of the pixels in the image. The effective focal spot size f_x, f_y of the X-ray source is calculated by $(\overline{EF} + \overline{GH})/M_{x,y}$, and magnification $M_{x,y}$ is calculated by $D_{x,y}/D_{real}$. The diameters D_x and D_y of the test object in width and length direction shall be measured at 50 % of the total image contrast (points B and C). The D_{real} is the real diameter of tungsten sphere.

Fig. 14 shows the recorded transverse size (f_x) and the longitudinal size (f_y) of the effective focal spot at varying U_{focus1} and U_{focus2}. In addition, an anode focal spot was simulated using CST at a focusing electrode voltage corresponding to that used in the experiment. The simulation results were then converted to the effective focal spot size according to the calculation of the tilt angle of the anode target.

As shown in Fig. 14(a) and (b), both f_x and f_y decrease initially and then increase with variations in U_{focus2}, with the smallest focal spot size occurring when U_{focus2} is approximately 700 V. The smallest focal spot size measured was 285 μm × 53 μm, with an anode current of 98 μA. The trends observed in the simulation calculations are consistent with the experimental results. Since X-ray intensity and image quality are correlated, it is imperative to remove the impact of current on the focal spot. The DC emission characteristics test findings indicate that raising the U_{focus1} will greatly increase the current and, in turn, the X-ray intensity. To maintain a consistent anode current when adjusting U_{focus1}, the filament current must be modified. In Fig. 14(c) and (d), both experimental and simulation results of f_x and f_y increase with increasing U_{focus2}. The results indicate that U_{focus1} caused a smaller range of focal spot variations than U_{focus2}. The focusing effect of the electron beam is more noticeable at the second focusing electrode because it is farther away from the cathode than the first focusing electrode.

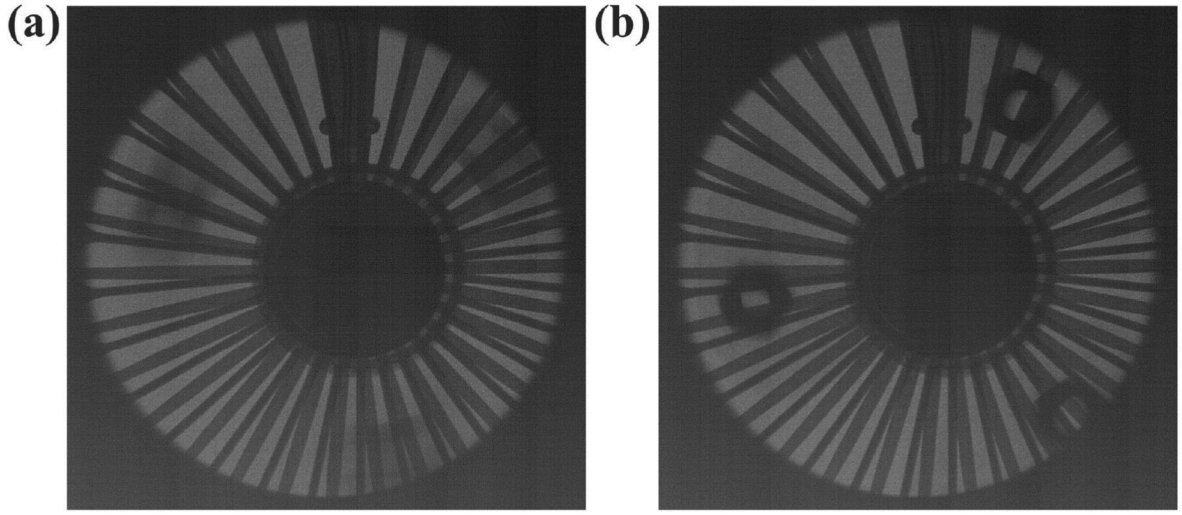

Fig. 16. Pulse imaging, (a)pulse width 200 μs (b) pulse width 50 μs.

3.2.4. Pulse emission test

The LYSO-SiPM we used in our experiments is a detector coupled with LYSO (Lutetium-yttrium Oyorthosilicate) and Silicon Photomultipliers. In this study, anode voltage is 25 kV, U_{focus1} is 300 V, U_{focus2} is 700 V and a sine voltage signal with an amplitude ranging from −13 V to 0 V was loaded on the grid, thereby controlling the emission of X-ray pulses. In Fig. 15, the blue waveform is the pulse voltage signal loaded on the grid, and the red waveform is the X-ray pulse signal detected by the LYSO-SiPM. The normalized amplitude was calculated [16] by 20ln (A/B), where A is the X-ray signal amplitude at the current frequency and B is the maximum value of the X-ray signal amplitude at all frequencies. Fig. 16 reflects the correspondence between amplitude and frequency. The X-ray output signal exhibits a good frequency response to the input signal. The output and input pulses can be well matched at 800 kHz. The pulse emission frequency limit of this X-ray source reached as high as 840 kHz. The signal waveform output from the detector is a convolution of the X-ray pulse signal and the detector time response. The correspondence between normalized amplitude and frequency is nonlinear.

3.2.5. Pulse imaging test

A rotating fan was imaged using pulsed X-rays. Metal blocks were fixed on the fan blade as markers. Under an anode voltage of 25 kV, we compared the quality of the images at different X-ray pulse widths, as shown in Fig. 16. The filament current was adjusted to maintain the same X-ray intensity. As shown in Fig. 16, the image obtained at a single pulse width of 50 μs is clearer than that obtained at 200 μs. The results indicate that shortening the pulse width makes it easier to capture instantaneous images. Consequently, it is possible to regulate the PMFX to produce fast pulses that allow clear imaging of the moving object while minimizing imaging artifacts.

4. Conclusion

In summary, a pulsed microfocus X-ray source is proposed by combining GMXT and focusing electrode, and its performance is tested in a laboratory dynamic vacuum system. Through NSGA-II optimization method, CST-MATLAB was used to optimize the parameters. Obtained by simulation, the minimum focal spot of the structure with two focusing electrodes is 45 μm × 25 μm and with three focusing electrodes is 6 μm × 20 μm. The experimentally measured minimum focal spot of the PMFX with two focusing electrodes is 285 μm × 53 μm at an anode current of 98 μA, and the pulse X-ray modulation frequency of 840 kHz is achieved, indicating that this structure is feasible as a scheme for the microfocus pulsed X-ray source. Additionally, the X-ray source was used to emit X-rays with a pulse width of 50 μs to take instant pictures of the fan in rotation. Further improving the pulse frequency and intensity and reducing the focal spot of the X-ray source is expected to achieve higher quality and faster imaging requirements.

CRediT authorship contribution statement

Jiaxin Bai: Writing – original draft, Visualization, Methodology, Formal analysis, Data curation. **Yunpeng Liu:** Writing – review & editing, Supervision, Methodology, Funding acquisition, Conceptualization. **Junxu Mu:** Writing – review & editing. **Sheng Lai:** Writing – review & editing. **Hao Yu:** Writing – review & editing. **Ao Xia:** Writing – review & editing. **Kang Wang:** Writing – review & editing. **Xiaobin Tang:** Writing – review & editing, Supervision, Resources.

Declaration of competing interest

The authors declare that they have no known competing financial interests or personal relationships that could have appeared to influence the work reported in this paper.

Acknowledgments

This work was supported by the National Natural Science Foundation of China (Grant No. 12375256) and the Fundamental Research Funds for the Central Universities (Grant No. NT2023012).

Data availability

Data will be made available on request.

References

[1] C. Zhao, K. Fezzaa, R.W. Cunningham, H. Wen, F. De Carlo, L. Chen, A.D. Rollett, T. Sun, Real-time monitoring of laser powder bed fusion process using high-speed X-ray imaging and diffraction, Sci. Rep. 7 (2017) 3602, https://doi.org/10.1038/s41598-017-03761-2.

[2] C. Tan, C. Tang, W. Huang, Q. Jin, Y. Du, Q. Luo, P. Wu, D. Liu, L. Zhang, C. Xu, Beam simulation and experiment of multi-focal spot electron gun for distributed X-ray sources, Nucl. Instrum. Methods Phys. Res. Sect. A Accel. Spectrom. Detect. Assoc. Equip. 920 (2019) 43–49, https://doi.org/10.1016/j.nima.2018.11.039.

[3] C. Kamezawa, T. Numano, Y. Kawabata, S. Inoue, M. Kawakami, H. Furukawa, K. Hyodo, W. Yashiro, Dynamic X-ray elastography: a new tool for characterizing soft materials, MRS Communications 11 (2021) 46–50, https://doi.org/10.1557/s43579-020-00004-w.

[4] S. Hang, Y. Liu, H. Li, X. Tang, D. Chen, Temporal characteristic analysis of laser-modulated pulsed X-ray source for space X-ray communication, Nucl. Instrum. Methods Phys. Res. Sect. A Accel. Spectrom. Detect. Assoc. Equip. 887 (2018) 18–26, https://doi.org/10.1016/j.nima.2018.01.031.

[5] S.M. Foreman, C. Kealhofer, G.E. Skulason, B.B. Klopfer, M.A. Kasevich, Ultrafast microfocus x-ray source based on a femtosecond laser-triggered tip, Ann. Phys. 525 (2013), https://doi.org/10.1002/andp.201200186.

[6] F. Zhou, G. Wu, B. Zhao, L. Sheng, J. Song, Y. Liu, Q. Yan, N. Deng, J. Zhao, An analog modulated simulation source for X-ray pulsar-based navigation, Wuli Xuebao/Acta Phys. Sin. 62 (2013), https://doi.org/10.7498/aps.62.119701.

[7] H. Mou, B. Li, Y. Cao, Transmission-type miniature micro-beam modulated X-ray source based on space application, Wuli Xuebao/Acta Phys. Sin. 65 (2016), https://doi.org/10.7498/aps.65.140703.

[8] X. Ma, B. Zhao, L. Sheng, Y. Liu, D. Liu, N. Deng, Grid-controlled emission source for space X-ray communication, Wuli Xuebao/Acta Phys. Sin. 63 (2014), https://doi.org/10.7498/aps.63.160701.

[9] S. Park, J.-T. Kang, J.-W. Jeong, J.-W. Kim, K.N. Yun, H. Jeon, E. Go, J.-W. Lee, Y. Ahn, J.-H. Yeon, S. Kim, Y.-H. Song, A fully closed nano-focus X-ray source with carbon nanotube field emitters, IEEE Electron Device Lett. 39 (2018) 1936–1939, https://doi.org/10.1109/LED.2018.2873727.

[10] G.Z. Yue, Q. Qiu, B. Gao, Y. Cheng, J. Zhang, H. Shimoda, S. Chang, J.P. Lu, O. Zhou, Generation of continuous and pulsed diagnostic imaging x-ray radiation using a carbon-nanotube-based field-emission cathode, Appl. Phys. Lett. 81 (2002) 355–357, https://doi.org/10.1063/1.1492305.

[11] M.U. Ghani, M.D. Wong, L. Ren, D. Wu, B. Zheng, JohnX. Rong, X. Wu, H. Liu, Characterization of continuous and pulsed emission modes of a hybrid micro focus x-ray source for medical imaging applications, Nucl. Instrum. Methods Phys. Res. Sect. A Accel. Spectrom. Detect. Assoc. Equip. 853 (2017) 70–77, https://doi.org/10.1016/j.nima.2017.02.030.

[12] X. Ma, B. Zhao, L. Sheng, Y. Liu, D. Liu, N. Deng, Grid-controlled emission source for space X-ray communication, Wuli Xuebao/Acta Phys. Sin. 63 (2014), https://doi.org/10.7498/aps.63.160701.

[13] H. Xuan, Y. Liu, P. Qiang, T. Su, X. Yang, L. Sheng, B. Zhao, Light-controlled pulsed X-ray tube with photocathode, Chinese Phys. B. (2021), https://doi.org/10.1088/1674-1056/abff1e.

[14] Z. Feng, Y. Liu, J. Mu, W. Chen, S. Lai, X. Tang, Optimization and testing of groove-shaped grid-controlled modulated X-ray tube for X-ray communication, Nucl. Instrum. Methods Phys. Res. Sect. A Accel. Spectrom. Detect. Assoc. Equip. 1026 (2022) 166218, https://doi.org/10.1016/j.nima.2021.166218.

[15] K. Deb, A. Pratap, S. Agarwal, T. Meyarivan, A fast and elitist multiobjective genetic algorithm: nsga-II, IEEE Trans. Evol. Computat. 6 (2002) 182–197, https://doi.org/10.1109/4235.996017.

[16] S. Cheng, L. Shen, J. Chen, Optimization of regional coverage reconnaissance satellite constellation by improved NSGA-II algorithm. 2008 International Conference on Intelligent Computation Technology and Automation, 2008, pp. 660–664, https://doi.org/10.1109/ICICTA.2008.322.

[17] L.-P. Wang, Y. Ren, Q.-C. Qiu, Survey on performance indicators for multi-objective evolutionary algorithms, Chin. J. Comput. (2021), https://doi.org/10.11897/SP.J.1016.2021.01590.

[18] S. Lai, X. Tang, Y. Liu, J. Mu, Z. Feng, K. Miao, X-ray high frequency pulse emission characteristic and application of CNT cold cathode x-ray source cathode x-ray source, Nanotechnology 33 (2022) 075201, https://doi.org/10.1088/1361-6528/ac378b.

[19] Non-destructive Testing—Characteristics of Focal Spots in Industrial X-Ray Systems for Use in Non-destructive Testing—Part 5: Measurement of the Effective Focal Spot Size of Mini and Micro Focus X-Ray Tubes, European Comittee for Standardization, CEN, September 1999. EN 12543-5:1999 E.